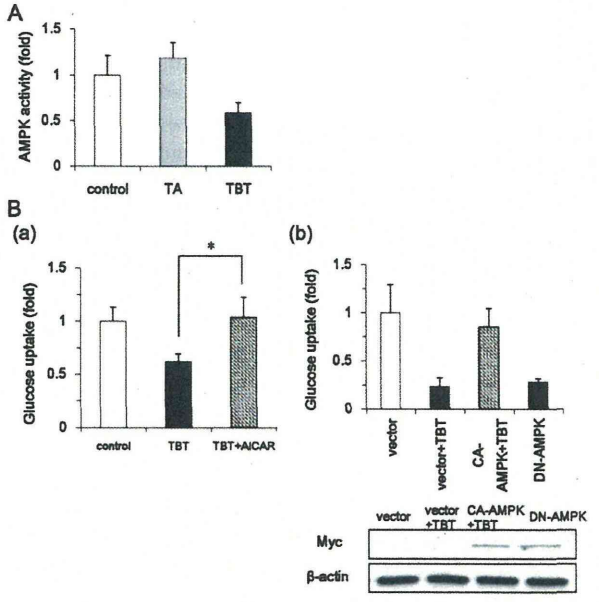

Fig. 3 Effect of AMPK on glucose uptake in NT2/D1 cells. (A) NT2/D1 cells were exposed to TBT or TA at 100 nM for 24 h. AICAR (0.5 mM) treatment was performed for 3 h. AMPK activity in the lysed cells was determined using a commercial assay kit. (B) NT2/D1 cells were exposed to TBT in the presence of 0.5 mM AICAR. (C) After overexpression of constitutively active (CA) mutants of AMPK, NT2/D1 cells were exposed to 100 nM TBT for 24 h, and glucose uptake assay was performed. After overexpression of dominant-negative (DN) mutants of AMPK, basal glucose uptake was tested. A glucose uptake assay was performed using the fluorescent glucose analog 2-NBDG. The fluorescence intensities of incorporated 2-NBDG were normalized to total cellular protein content. $^*P < 0.05$.

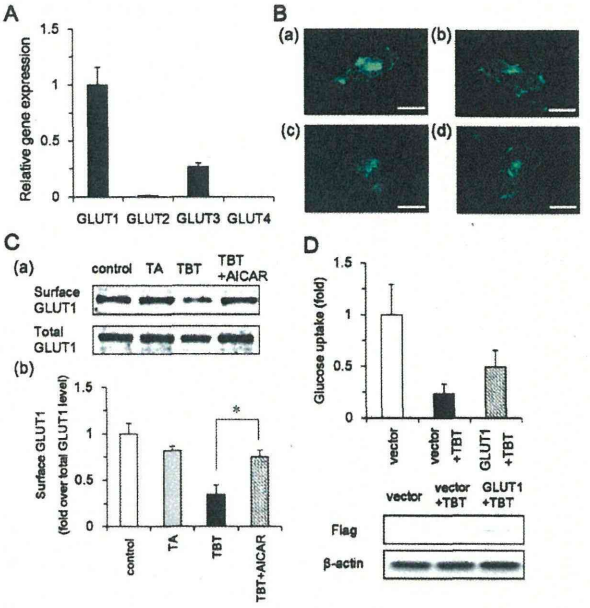

Fig. 4 Effect of TBT exposure on GLUT1 localization in NT2/D1 cells. (A) Expression of GLUT family by real-time PCR in NT2/D1 cells. Relative changes were determined by normalizing to RPL13. (B) After exposure to 100 nM TBT for 24 h, NT2/D1 cells were immunostained with anti-GLUT1 polyclonal antibodies. (a) Control, (b) 100 nM TA, (c) 100 nM TBT, and (d) 100 nM TBT + 0.5 mM AICAR. (Bar = 25 μm). (C) (a) NT2/D1 cell surface proteins were biotinylated using Sulfo-NHS-SS-Biotin, and then lysed. After precipitation with streptavidin beads, biotinylated proteins were analyzed by western blotting using anti-GLUT1 antibodies. Total GLUT1 protein was detected in cell lysate. (b) The relative density of bands was quantified with ImageJ software. Cell surface GLUT1 levels were normalized to total GLUT1 levels. (D) After overexpression of GLUT1, NT2/D1 cells were exposed to 100 nM TBT for 24 h, and glucose uptake assay was performed using the fluorescent glucose analog 2-NBDG. The fluorescence intensities of incorporated 2-NBDG were normalized to total cellular protein content. $^*P < 0.05$.

TBT suppressed the growth curve, but the total cell number did not alter throughout the time-course experiment (Fig. 1B). These data suggest that exposure to 100 nM TBT induced growth arrest in the cells without causing cell death.

Glucose provides metabolic energy for cell growth and it is incorporated by glucose transporters.[17] To examine the mechanism by which TBT induces growth arrest at low concentrations, we determined the glucose-6-phosphate, a major metabolite in glycolysis. We found that exposure to 100 nM TBT reduced the amount of glucose-6-phosphate (Fig. 2A). Fructose-6-phosphate, which is produced by isomerization of glucose 6-phosphate, also reduced by TBT. To check whether the decrease in glucose-6-phosphate is induced by inhibition of glucose transport, we examined the activity of glucose uptake by using 2-NBDG, a fluorescently labeled 2-deoxyglucose. Similar to the cell growth, glucose uptake was significantly inhibited by 100 nM TBT, not by 30 nM TBT (Fig. 2B). TA had little effect on glucose uptake. To examine whether the inhibition is regulated by transcription, we tested the effect of short-term exposure. Exposure to TBT for 1 h suppressed glucose uptake (Fig. S1, ESI†), suggesting that gene expression is not involved in the effect of TBT. Since TBT has been shown to activate transcriptional activity of peroxisome proliferator-activated receptor γ (PPARγ),[27,28] we tested the effect of the PPARγ agonist rosiglitazone on the glucose uptake. Treatment with rosiglitazone increased glucose uptake (Fig. S2, ESI†), suggesting that PPARγ is not involved in TBT-induced inhibition of glucose uptake. Furthermore, we examined the activity of hexokinase, which catalyzes the phosphorylation of glucose into glucose-6-phosphate. As shown in Fig. 2C, hexokinase activity was not significantly altered by TBT. Exposure to TA also produced similar results. These data suggest that TBT exposure decreases the amount of glycolytic metabolites *via* inhibition of glucose transport.

AMP-activated protein kinase (AMPK) is known to regulate the translocation of a glucose transporter (GLUT) to the plasma membrane.[29] We examined whether AMPK is involved in the inhibition of glycolytic systems by TBT exposure. Exposure to 100 nM TBT reduced AMPK activity (Fig. 3A). In contrast, TA had little effect on AMPK. In addition, treatment with AICAR (a potent AMPK activator) recovered the inhibitory effect of TBT on glucose uptake (Fig. 3B). To confirm the effect of AICAR, we examined the effect of constitutively active (CA) mutants of AMPK. Similar to the treatment with AICAR, overexpression of CA-AMPK recovered the inhibitory effect of TBT on glucose uptake. Overexpression of dominant-negative mutants of AMPK reduced the basal level of glucose uptake, suggesting that

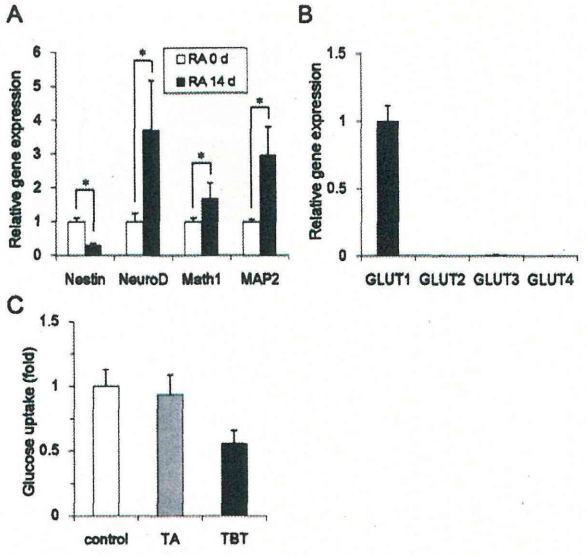

Fig. 5 Effect of neuronal induction on glucose uptake under TBT exposure in NT2/D1 cells. (A) To induce neuronal differentiation, NT2/D1 cells were treated with 10 μM RA for 14 days. The relative expression of neuronal markers (NeuroD, Math1, and MAP2) and a marker of undifferentiation (nestin) were measured by real-time-PCR. The relative changes were normalized to RPL13. (B) Expressions of members of the GLUT family were measured by real-time PCR in differentiated NT2/D1 cells. Relative changes were determined by normalizing to RPL13. (C) After exposure to 100 nM TBT for 24 h, glucose uptake was measured in differentiated cells. The fluorescence intensities of intracellularly incorporated 2-NBDG were measured and normalized to the total cellular protein levels. $^{*}P < 0.05$.

glucose uptake is AMPK-dependent in NT2/D1 cells. Taken together, these data suggest that TBT exposure suppresses glucose uptake through the inhibition of AMPK activity.

We next examined the mechanism by which AMPK regulates glucose uptake in NT2/D1 cells. Real-time PCR analysis showed that GLUT1 was a major subtype in NT2/D1 cells (Fig. 4A). Since TBT exposure did not affect gene expression of GLUT1 (data not shown), we examined GLUT1 localization by immunohistochemistry. Expression of GLUT1 was observed at the plasma membrane and in the intracellular segment (Fig. 4B). Exposure with TBT reduced the cell surface expression of GLUT1. Treatment with AICAR recovered the inhibitory effect of TBT. To confirm these observations using microscopy, we labeled cell surface-bound GLUT1 by biotinylation of cell surface proteins (Fig. 4C). Using this approach, we determined that TBT exposure reduced the amount of cell surface-bound GLUT1. AICAR reversed this inhibitory effect of TBT. Furthermore, overexpression of GLUT1 partially recovered the TBT-induced inhibition of glucose uptake (Fig. 4D). These data suggest that TBT inhibits glucose uptake mediated by cell surface translocation of GLUT1, a process dependent on AMPK.

To examine whether the effect of TBT was selective for embryonic cells, we used NT2/D1 cells differentiated by retinoic acid.[30] Real-time PCR analysis revealed that RA-treated NT2/D1 cells showed upregulated expression of markers of differentiation (NeuroD, Math1, MAP2) and downregulated expression of a marker of undifferentiation (nestin), confirming the induction of differentiation (Fig. 5A). Real-time PCR confirmed that GLUT1 is a major subtype in the differentiated NT2/D1 cells (Fig. 5B). Furthermore, exposure to 100 nM TBT also reduced glucose uptake in differentiated NT2/D1 cells. In contrast, TA had little effect (Fig. 5C). These data suggest that TBT suppresses glucose uptake in both undifferentiated and differentiated cells.

Discussion

In the present study, we showed that the glycolytic pathway is a novel target of TBT toxicity in human embryonic carcinoma cells. We showed that TBT suppresses AMPK-dependent glucose uptake, and thereby, the amount of glucose-6-phosphate. The inhibitory effects of TBT on glycolytic systems would lead to growth arrest in the cells. Fig. 6 shows a proposed model of TBT-induced toxicity, based on the data observed in our study.

Our studies showed that treatment with 1 μM TBT resulted in the death of human embryonic carcinoma cells (Fig. 1). Consistent with these observations, previous studies have shown that micromolar levels of TBT induce apoptosis in various cells such as human amnion cells,[31] hepatocytes,[32] and neutrophils.[33] In contrast, exposure to 100 nM TBT resulted in neither growth arrest nor cell death. Therefore, we focused on intracellular metabolites as potential mediators of TBT-induced growth arrest. We found that exposure to nanomolar levels of TBT affects the intracellular metabolic balance and decreases the amount of glucose metabolites (Fig. 2). A previous report showed that the organotin compounds such as TBT might be present in human blood at nanomolar levels.[16] Glucose metabolism analysis revealed novel toxic mechanisms

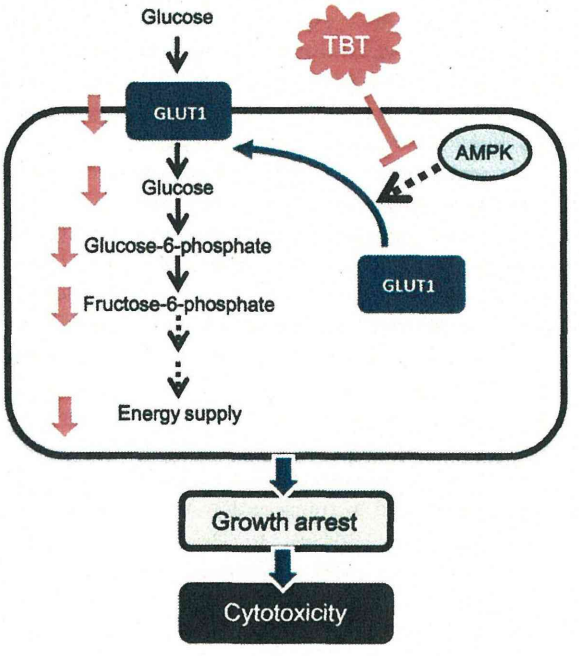

Fig. 6 Proposed model of TBT toxicity in human embryonic carcinoma cells.

for the toxicity of nanomolar levels of TBT. Thus, the glycolytic pathway might account for the unknown toxic mechanism induced by heavy metal exposure.

Our data suggest that the target molecule of TBT toxicity is GLUT1, a major subtype of GLUT in NT2/D1 cells (Fig. 4). Since the expression of GLUT1 is observed in a broad range of cell types, the toxicity of TBT may also be observed in other cells. For example, we showed that TBT reduces glucose uptake in differentiated NT2/D1 cells, which express GLUT1 (Fig. 5). Thus, it is possible that TBT induces toxicity in mature neurons *via* inhibition of GLUT function.

We showed that TBT decreases AMPK activity, one of the GLUT regulators, in NT2/D1 cells (Fig. 3). In addition, overexpression of AMPK or the AMPK activator restored the glucose uptake, confirming that AMPK is a possible target of TBT. In contrast, 500 nM TBT has been shown to increase AMPK phosphorylation in rat cortical neurons.[34] This discrepancy might be due to the concentration of TBT or different types of cells.

Several studies suggest that TBT directly interacts with target enzymes. TBT at a concentration of 10–100 nM has been shown to act as an agonist of PPARγ and the retinoid X receptor (RXR) because of its higher binding affinity compared to intrinsic ligands. Other studies reported that micromolar concentrations of TBT inhibit F1F0 ATP synthase and 11β-hydroxysteroid dehydrogenase by direct interaction.[35,36] Therefore, TBT can bind to multiple targets with broad specificity. It is possible that TBT also interacts with AMPK. On the other hand, calmodulin-dependent protein kinase II (CaMK II) and serine–threonine liver kinase B1 (LKB1) have been shown to phosphorylate AMPK and cause subsequent activation of glucose transport.[29] Furthermore, there may be an additional signaling molecule between TBT and AMPK. It remains to be elucidated how TBT regulates AMPK in embryonic carcinoma cells.

Nanomolar levels of TBT may interact with several targets in other types of cells, such as PPARγ, RXR, and α-amino-3-hydroxy-5-methylisoxazole-4-propionic acid (AMPA) receptors 2 (GluR2). Since rosiglitazone, a PPARγ agonist, increased glucose transport in NT2/D1 cells (Fig. S2, ESI†), it is unlikely that TBT inhibits glucose transport *via* PPARγ in the cells. RXR transgenic mice have been shown to exhibit an increase in GLUT1 expression in the skeletal muscles.[37] Since the expression level of GLUT1 was not changed by TBT exposure in NT2/D1 cells and the inhibitory effect of glucose uptake was observed after a 1 h treatment with TBT, it is likely that RXR is not involved in TBT-mediated alteration of glucose transport. Moreover, exposure to nanomolar levels of TBT has been reported to decrease the mRNA expression of GluR2 in cultured rat cortical neurons.[38] Although NT2/D1 cells do not express GluR2, it is possible that GluR2 may be a target in the differentiated NT2/D1 cells. Further studies are required to examine these targets other than the glycolytic pathway.

Conclusions

We found that exposure to nanomolar levels of TBT mainly targets the glycolytic systems in human embryonic carcinoma cells. Thus, glycolytic systems may be a good target for previously unknown mechanisms of toxicity induced by metal exposure at nanomolar levels.

Conflict of interest

The authors declare that there are no conflicts of interest.

List of abbreviations

AMPK	AMP-activated protein kinase
GLUT	glucose transporter
RA	all-trans retinoic acid
PPARγ	peroxisome proliferator-activated receptor γ
TA	tin acetate
TBT	tributyltin

Acknowledgements

We would like to thank Dr Rathmell and Dr Carling for providing the materials. This study was supported in part by a Health and Labour Sciences Research Grant from the Ministry of Health, Labour and Welfare, Japan (Y. Ka.), a grant from the Program for Promotion of Fundamental Studies in Health Sciences of the National Institute of Biomedical Innovation (NIBIO) (No. 09-02 to Y. Ka.), Grants-in-Aid for Scientific Research (No. 23590322 to Y. Ka. and No. 23310047 to Y. Ko.) from the Japan Society for the Promotion of Science, and a grant from the Smoking Research Foundation (Y. Ka.).

References

1 H. L. Needleman, C. Gunnoe, A. Leviton, R. Reed, H. Peresie, C. Maher and P. Barrett, Deficits in psychologic and classroom performance of children with elevated dentine lead levels, *N. Engl. J. Med.*, 1979, **300**, 689–695.
2 G. Winneke, Developmental aspects of environmental neurotoxicology: lessons from lead and polychlorinated biphenyls, *J. Neurol. Sci.*, 2011, **308**, 9–15.
3 L. G. Costa, M. Aschne, A. Vitalone, T. Syversen and O. P. Soldin, Developmental neuropathology of environmental agents, *Annu. Rev. Pharmacol. Toxicol.*, 2004, **44**, 87–110.
4 J. Dobbing, *Vulnerable periods in developing brain*, in *Appl. Neurochem.*, ed. A. N. Davison and J. Dobbing, Davis, Philadelphia, 1968, pp. 287–316.
5 P. M. Rodier, Developing brain as a target of toxicity, *Environ. Health Perspect.*, 1995, **103**(suppl 6), 73–76.
6 D. Rice and S. Barone Jr, Critical periods of vulnerability for the developing nervous system: evidence from humans and animal models, *Environ. Health Perspect.*, 2000, **108**(suppl 3), 511–533.
7 H. Asakawa, M. Tsunoda, T. Kaido, M. Hosokawa, C. Sugaya, Y. Inoue, Y. Kudo, T. Satoh, H. Katagiri, H. Akita, M. Saji, M. Wakasa, T. Negishi, T. Tashiro and Y. Aizawa, Enhanced

inhibitory effects of TBT chloride on the development of F1 rats, *Arch. Environ. Contam. Toxicol.*, 2010, **58**, 1065–1073.
8 S. Gómez-Ruiz, G. N. Kaluderović, S. Prashar, E. Hey-Hawkins, A. Erić, Z. Zizak and Z. D. Juranić, Study of the cytotoxic activity of di and triphenyltin(IV) carboxylate complexes, *J. Inorg. Biochem.*, 2008, **102**, 2087–2096.
9 L. Rocamora-Reverte, E. Carrasco-García, J. Ceballos-Torres, S. Prashar, G. N. Kaluđerović, J. A. Ferragut and S. Gómez-Ruiz, Study of the anticancer properties of tin(IV) carboxylate complexes on a panel of human tumor cell lines, *ChemMedChem*, 2012, **7**, 301–310.
10 A. González, E. Gómez, A. Cortés-Lozada, S. Hernández, T. Ramírez-Apan and A. Nieto-Camacho, Heptacoordinate tin(IV) compounds derived from pyridine Schiff bases: synthesis, characterization, *in vitro* cytotoxicity, anti-inflammatory and antioxidant activity, *Chem. Pharm. Bull.*, 2009, **57**, 5–15.
11 Y. Kotake, Molecular mechanisms of environmental organotin toxicity in mammals, *Biol. Pharm. Bull.*, 2012, **35**, 1876–1880.
12 T. Noda, S. Morita, T. Yamano, M. Shimizu, T. Nakamura, M. Saitoh and A. Yamada, Teratogenicity study of tri-*n*-butyltin acetate in rats by oral administration, *Toxicol. Lett.*, 1991, **55**, 109–115.
13 A. T. Gardlund, T. Archer, K. Danielsen, B. Danielsson, A. Frederiksson, N. G. Lindquist, H. Lindstrom and J. Luthman, Effects of prenatal exposure to tributyltin and trihexyltin on behavior in rats, *Neurotoxicol. Teratol.*, 1991, **13**, 99–105.
14 Q. Li, M. Osada, K. Takahashi, T. Matsutani and K. Mori, Accumulation and depuration of tributyltin oxide and its effect on the fertilization and embryonic development in the pacific oyster, *Crassostrea gigas*, *Bull. Environ. Contam. Toxicol.*, 1997, **58**, 489–496.
15 Y. Nakatsu, Y. Kotake, K. Komasaka, H. Hakozaki, R. Taguchi, T. Kume, A. Akaike and S. Ohta, Glutamate excitotoxicity is involved in cell death caused by tributyltin in cultured rat cortical neurons, *Toxicol. Sci.*, 2006, **89**, 235–242.
16 M. M. Whalen, B. G. Loganathan and K. Kannan, Immunotoxicity of environmentally relevant concentrations of butyltins on human natural killer cells *in vitro*, *Environ. Res. Lett.*, 1999, **81**, 108–116.
17 L. Pellerin, Food for thought: the importance of glucose and other energy substrates for sustaining brain function under varying levels of activity, *Diabetes Metab.*, 2010, **36**, S59–S63.
18 K. Barnes, J. C. Ingram, O. H. Porras, L. F. Barros, E. R. Hudson, L. G. Fryer, F. Foufelle, D. Carling, D. G. Hardie and S. A. Baldwin, Activation of GLUT1 by metabolic and osmotic stress: potential involvement of AMP-activated protein kinase (AMPK), *J. Cell Sci.*, 2002, **115**, 2433–2442.
19 M. Jing, V. K. Cheruvu and F. Ismail-Beigi, Stimulation of glucose transport in response to activation of distinct AMPK signaling pathways, *Am. J. Physiol.: Cell Physiol.*, 2008, **295**, C1071–C1082.
20 B. Kunievsky, J. Pretsky and E. Yavin, Transient rise of glucose uptake in the fetal rat brain after brief episodes of intrauterine ischemia, *Dev. Neurosci.*, 1994, **16**, 313–320.
21 K. Matsumoto, S. Akazawa, M. Ishibashi, R. A. Trocino, H. Matsuo, H. Yamasaki, Y. Yamaguchi, S. Nagamatsu and S. Nagataki, Abundant expression of GLUT1 and GLUT3 in rat embryo during the early organogenesis period, *Biochem. Biophys. Res. Commun.*, 1995, **209**, 95–102.
22 P. J. Jensen, J. D. Gitlin and M. O. Carayannopoulos, GLUT1 deficiency links nutrient availability and apoptosis during embryonic development, *J. Biol. Chem.*, 2006, **281**, 13382–13387.
23 Y. Kanda and Y. Watanabe, Thrombin-induced glucose transport *via* Src-p38 MAPK pathway in vascular smooth muscle cells, *Br. J. Pharmacol.*, 2005, **146**, 60–67.
24 T. Soga, Y. Ueno, H. Naraoka, Y. Ohashi, M. Tomita and T. Nishioka, Simultaneous determination of anionic intermediates for *Bacillus subtilis* metabolic pathways by capillary electrophoresis electrospray ionization mass spectrometry, *Anal. Chem.*, 2002, **74**, 2233–2239.
25 Y. Kanda and Y. Watanabe, Adrenaline increases glucose transport *via* a Rap1-p38MAPK pathway in rat vascular smooth muscle cells, *Br. J. Pharmacol.*, 2007, **151**, 476–482.
26 N. Hiarta, Y. Sekinoa and Y. Kanda, Nicotine increases cancer stem cell population in MCF-7 cells, *Biochem. Biophys. Res. Commun.*, 2010, **403**, 138–143.
27 T. Kanayama, N. Kobayashi, S. Mamiya, T. Nakanishi and J. Nishikawa, Organotin compounds promote adipocyte differentiation as agonists of the peroxisome proliferator-activated receptor gamma/retinoid X receptor pathway, *Mol. Pharmacol.*, 2005, **67**, 766–774.
28 F. Grün, H. Watanabe, Z. Zamanian, L. Maeda, K. Arima, R. Cubacha, D. M. Gardiner, J. Kanno, T. Iguchi and B. Blumberg, Endocrine-disrupting organotin compounds are potent inducers of adipogenesis in vertebrates, *Mol. Endocrinol.*, 2006, **20**, 2141–2155.
29 D. G. Hardie, F. A. Ross and S. A. Hawley, AMPK: a nutrient and energy sensor that maintains energy homeostasis, *Nat. Rev. Mol. Cell Biol.*, 2012, **13**, 251–262.
30 S. J. Pleasure, C. Page and V. M. Lee, Pure, postmitotic, polarized human neurons derived from NTera 2 cells provide a system for expressing exogenous proteins in terminally differentiated neurons, *J. Neurosci.*, 1992, **12**, 1802–1815.
31 X. Zhu, M. Xing, J. Lou, X. Wang, W. Fu and L. Xu, Apoptotic related biochemical changes in human amnion cells induced by tributyltin, *Toxicology*, 2007, **230**, 45–52.
32 M. Grondin, M. Marion, F. Denizeau and D. A. Averill-Bate, Tributyltin induces apoptotic signaling in hepatocytes through pathways involving the endoplasmic reticulum and mitochondria, *Toxicol. Appl. Pharmacol.*, 2007, **222**, 57–68.
33 V. Lavastre and D. Girard, Tributyltin induces human neutrophil apoptosis and selective degradation of cytoskeletal proteins by caspases, *J. Toxicol. Environ. Health, Part A*, 2002, **65**, 1013–1024.

34 Y. Nakatsu, Y. Kotake, A. Hino and S. Ohta, Activation of AMP-activated protein kinase by tributyltin induces neuronal cell death, *Toxicol. Appl. Pharmacol.*, 2008, **230**, 358–363.
35 C. von Ballmoos, J. Brunner and P. Dimroth, The ion channel of F-ATP synthase is the target of toxic organotin compounds, *Proc. Natl. Acad. Sci. U. S. A.*, 2004, **101**, 11239–11244.
36 A. G. Atanasov, L. G. Nashev, S. Tam, M. E. Baker and A. Odermatt, Organotins disrupt the 11β-hydroxysteroid dehydrogenase type 2-dependent local inactivation of glucocorticoids, *Environ. Health Perspect.*, 2005, **113**, 1600–1606.
37 S. Sugita, Y. Kamei, F. Akaike, T. Suganami, Ṡ. Kanai, M. Hattori, Y. Manabe, N. Fujii, T. Takai-Igarashi, M. Tadaishi, J. Oka, H. Aburatani, T. Yamada, H. Katagiri, S. Kakehi, Y. Tamura, H. Kubo, K. N. S. Miura, O. Ezaki and Y. Ogawa, Increased systemic glucose tolerance with increased muscle glucose uptake in transgenic mice overexpressing RXRγ in skeletal muscle, *PLoS One*, **6**, e20467.
38 Y. Nakatsu, Y. Kotake Y, T. Takishit and S. Ohta, Long-term exposure to endogenous levels of tributyltin decreases GluR2 expression and increases neuronal vulnerability to glutamate, *Toxicol. Appl. Pharmacol.*, 2009, **240**, 292–298.

The Journal of Toxicological Sciences (J. Toxicol. Sci.)
Vol.39, No.2, 285-292, 2014

Toxicomics Report

Proteomic analysis of ethanol-induced embryotoxicity in cultured post-implantation rat embryos

Makoto Usami[1], Katsuyoshi Mitsunaga[2], Tomohiko Irie[1], Atsuko Miyajima[3] and Osamu Doi[4]

[1]Division of Pharmacology, National Institute of Health Sciences, 1-18-1 Kamiyoga, Setagaya, Tokyo, 158-8501, Japan
[2]School of Pharmaceutical Sciences, Toho University, 2-2-1 Miyama, Funabshi, Chiba, 274-8510, Japan
[3]Division of Medical Devices, National Institute of Health Sciences, 1-18-1 Kamiyoga, Setagaya, Tokyo, 158-8501, Japan
[4]Laboratory of Animal Reproduction, United Graduate School of Agricultural Science, Gifu University, 1-1 Yanagido, Gifu, 501-1193, Japan

(Received November 9, 2013; Accepted December 18, 2013)

ABSTRACT — Protein expression changes were examined in day 10.5 rat embryos cultured for 24 hr in the presence of ethanol by using two-dimensional electrophoresis and mass spectrometry. Exposure to ethanol resulted in quantitative changes in many embryonic protein spots (16 decreased and 28 increased) at *in vitro* embryotoxic concentrations (130 and 195 mM); most changes occurred in a concentration-dependent manner. For these protein spots, 17 proteins were identi ed, including protein disul de isomerase A3, alpha-fetoprotein, phosphorylated co lin-1, and serum albumin. From the gene ontology classi cation and pathway mapping of the identi ed proteins, it was found that ethanol affected several biological processes involving oxidative stress and retinoid metabolism.

Key words: Ethanol, Embryotoxicity, Proteomics, Rat

INTRODUCTION

Developmental toxicology is a rapidly growing area of proteomics; it is expected to provide mechanistic insights and protein biomarkers for the safety evaluation of chemicals (Usami and Mitsunaga, 2011). For example, expression changes in actin-binding proteins were considered to be involved in selenate embryotoxicity in the rat whole embryo culture (Usami *et al.*, 2008). Differences in strain sensitivity to cadmium-induced teratogenicity were related to unfolded protein response process and actin polymerization in the mouse limb-bud culture (Chen *et al.*, 2008). Furthermore, based on cluster analysis of proteins with expression changes in the embryonic stem cell test, chemicals were classi ed into highly embryotoxic and non- or weakly embryotoxic (Groebe *et al.*, 2010). It is thus important to accumulate proteomic analysis data in the eld of developmental toxicology. In the present study, protein expression changes in day 10.5 rat embryos cultured for 24 hr in the presence of ethanol, a well-known developmental toxicant, were examined by two-dimensional electrophoresis (2-DE) and mass spectrometry (MS).

MATERIAL AND METHODS

Embryo culture and ethanol treatment

Day 10.5 embryos (plug day = day 0.5) of Wistar rats (Crlj: WI, Charles River Laboratories Japan, Inc., Kanagawa, Japan) were cultured for 24 hr (Usami *et al.*, 2008). Ethanol was diluted in Hank's balanced salt solution in two-fold and added to the culture medium composed of 100% rat serum at concentrations of 0, 65, 130, and 195 mM. Medium-sized cultured embryos (four embryos per treatment group) were selected for subsequent protein analyses. All animal experiments were carried out according to the guidelines for animal use of the National Institute of Health Sciences.

2-DE and MS analyses of embryonic protein

The analyses of 2-DE gels (one embryo per gel, four gels per treatment group) were carried out as previously reported (Usami *et al.*, 2009), except that the gels were stained with a uorescent dye (Flamingo gel stain, Bio-Rad, Hercules, CA, USA) and scanned with a laser scanner (FLA-5100, GE Healthcare UK Ltd., Amersham Place, Little Chalfont, UK) at an excitation wavelength of

Correspondence: Makoto Usami (E-mail: usami@nihs.go.jp)

473 nm. Quantitative differences in protein spots of more than 1.5-fold with statistical signi cance by the *t*-test at 5% probability level between the control and 195 mM ethanol groups, were regarded as ethanol-induced protein expression changes.

Classification and mapping of identified proteins

NCBInr GI numbers of the identified proteins were mapped to UniProtKB AC, and gene ontology (GO) terms were assigned using the UniProt web site (http://www.uniprot.org/) (Jain *et al.*, 2009; The UniProt Consortium, 2011). The occurrence of the GO terms (76 biological processes) of the proteins was counted with the CateGOrizer web tool in the "MGI_GO_slim2" ancestor terms using the multiple count method (http://www.animalgenome.org/tools/catego/) (Hu *et al.*, 2008). UniProtKB ACs of the proteins were queried against the KEGG PATHWAY for *Rattus norvegicus* with the KEGG Mapper on the GenomeNet web site (http://www.genome.jp/en/).

RESULTS

Effects of ethanol on the growth of cultured rat embryos

Ethanol inhibited the growth of cultured embryos at concentrations of 130 mM or higher in a concentration-dependent manner (Table 1). Deformed organs included branchial arch, heart, neural tube, optic vesicle, otic vesicle, somite, and tail (Fig. 1), which is in agreement with previous reports (Giavini *et al.*, 1992; Zhou *et al.*, 2011). Compared to blood ethanol levels found in humans, these embryotoxic ethanol concentrations are rather high; however, an ethanol concentration of 150 mM can be observed after acute alcohol intake in chronic alcoholics and 200 mM of ethanol has often been used in *in vitro* toxicological experiments (Li and Kim, 2003; Szabo *et al.*, 1994; Wentzel and Eriksson, 2008).

Effects of ethanol on embryonic protein expression

About 900 protein spots were matched through sixteen 2-DE gels (four gels per experimental group). Quality changes, i.e., appearance or disappearance, in the

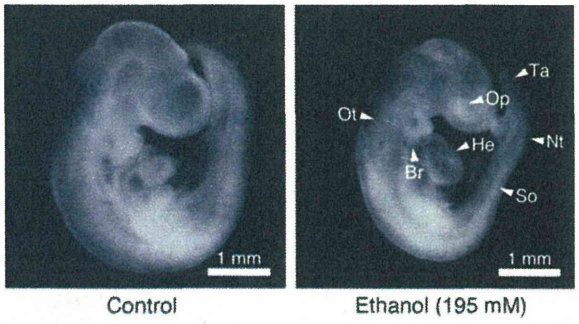

Fig. 1. Appearance of rat embryos cultured in the presence of ethanol. Rat embryos at the end of 24-hr culture are shown after removal of the embryonic membranes. Arrowheads indicate deformed organs. Br, branchial arch; He, heart; Nt, neural tube; Op, optic vesicle; Ot, otic vesicle; So, somite; Ta, tail.

Table 1. Growth of day 10.5 rat embryos cultured in the presence of ethanol

	Ethanol (mM)			
	0 (Control)	65	130	195
No. of embryos	6	5	6	5
No. of viable embryos	6 (100%)	5 (100%)	6 (100%)	5 (100%)
Crown-rump length (mm)	4.11 ± 0.15	3.99 ± 0.17	3.72 ± 0.29*	3.25 ± 0.28**
Head length (mm)	2.23 ± 0.11	2.16 ± 0.14	2.01 ± 0.22	1.74 ± 0.35**
No. of somite pairs	26.7 ± 0.52	26.4 ± 0.55	24.5 ± 2.81	21.2 ± 2.49**
No. of embryos with deformed organ	0	0	3 (50%)	5 (100%)**
Branchial arch	0	0	2 (33%)	4 (80%)*
Heart	0	0	1 (17%)	3 (60%)
Neural tube	0	0	2 (33%)	2 (40%)
Optic vesicle	0	0	2 (33%)	5 (100%)**
Otic vesicle	0	0	2 (33%)	5 (100%)**
Somite	0	0	3 (50%)	5 (100%)**
Tail	0	0	2 (33%)	4 (80%)*

Embryos were cultured for 24 hr by the roller method. Asterisks indicate statistically signi cant differences compared to the control group identi ed by Dunnett's multiple comparison test or Fisher's exact test (* $p < 0.05$; ** $p < 0.01$).

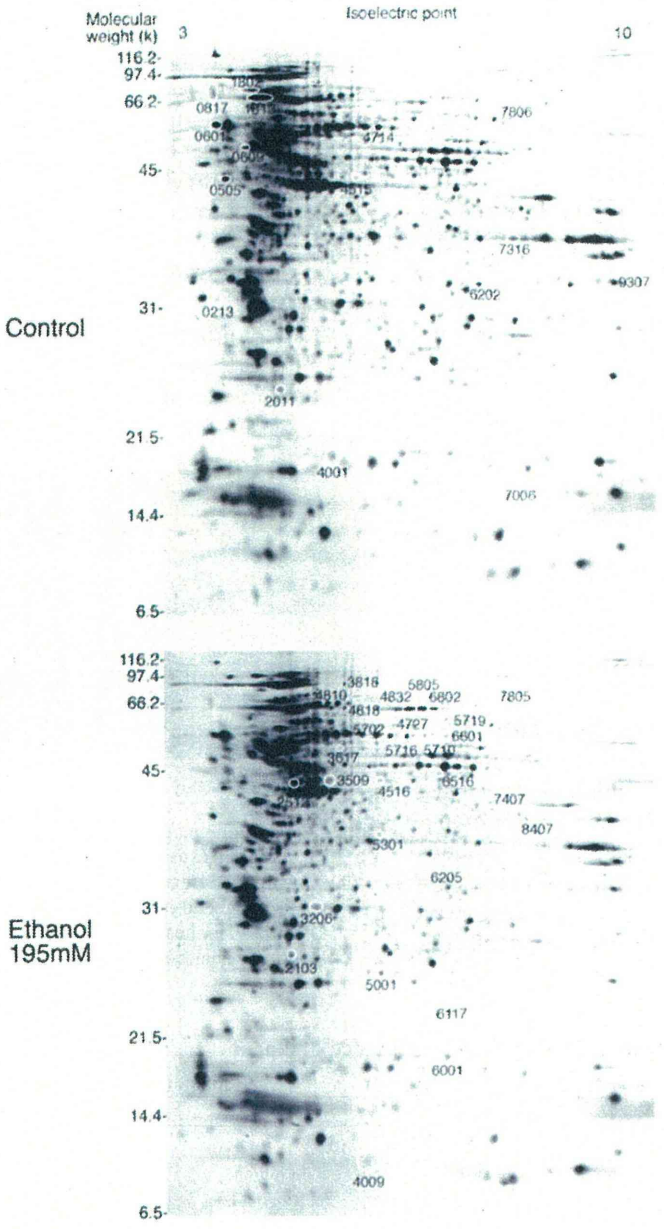

Fig. 2. Two-dimensional electrophoresis pattern of proteins from rat embryos cultured in the presence of ethanol. Representative gels are shown for the control and ethanol (195 mM) groups. Proteins with ethanol-induced expression changes are indicated by circles with standard spot numbers (SSPs); decreased proteins are indicated in the "control" gel (top) and increased ones in the "ethanol" gel (bottom).

protein spots were not observed. Ethanol-induced quantitative changes were noted in 44 spots, i.e., 16 spots were decreased and 28 spots were increased by 1.5-fold or more. The differences between the 195 mM ethanol group and the control group were signi cant and occurred for most proteins in a concentration-dependent manner (Figs. 2 and 3). Of these spots, 23 were analyzed by MS, resulting in the identi cation of 7 proteins that were decreased (Table 2) and 11 proteins that were increased (Table 3). Some proteins that were increased, e.g., alpha-fetopro-

Table 2. Proteins whose expression was decreased and their GO terms identi ed by two-dimensional electrophoresis analysis of rat embryos cultured in the presence of ethanol

SSP	Protein Name	UniProtKB AC	GO term for Biological Process
0505	Protein SET	Q63945	GO:0006334 nucleosome assembly
0601	Nucleosome assembly protein 1-like 1	Q9Z2G8	GO:0006334 nucleosome assembly
0817	Myristoylated alanine-rich C-kinase substrate	P30009	n.a.
1802	78 kDa glucose-regulated protein	P06761	GO:0006916 anti-apoptosis GO:0006983 ER overload response GO:0006987 activation of signaling protein activity involved in unfolded protein response GO:0021589 cerebellum structural organization GO:0021680 cerebellar Purkinje cell layer development GO:0030512 negative regulation of transforming growth factor beta receptor signaling pathway GO:0031398 positive regulation of protein ubiquitination GO:0042149 cellular response to glucose starvation GO:0043066 negative regulation of apoptotic process GO:0043154 negative regulation of cysteine-type endopeptidase activity involved in apoptotic process GO:0051603 proteolysis involved in cellular protein catabolic process
1813	Heat shock cognate 71 kDa protein	P63018	GO:0006351 transcription, DNA-dependent GO:0006355 regulation of transcription, DNA-dependent GO:0006950 response to stress GO:0045892 negative regulation of transcription, DNA-dependent GO:0051085 chaperone mediated protein folding requiring cofactor GO:0061077 chaperone-mediated protein folding
2011	Uncharacterized protein	D3ZRS6	n.a.
4714	Protein disul de-isomerase A3	P11598	GO:0006662 glycerol ether metabolic process GO:0043065 positive regulation of apoptotic process GO:0045454 cell redox homeostasis

n.a., not available.

Table 3. Proteins whose expression was increased and their GO terms identi ed by two-dimensional electrophoresis analysis of rat embryos cultured in the presence of ethanol

SSP	Protein Name	UniProtKB AC	GO term for Biological Process
2103	Myosin light chain 3	P16409	GO:0002026 regulation of the force of heart contraction GO:0006936 muscle contraction GO:0006942 regulation of striated muscle contraction GO:0007519 skeletal muscle tissue development GO:0055010 ventricular cardiac muscle tissue morphogenesis GO:0060048 cardiac muscle contraction
2512	BWK4 AND Eukaryotic initiation factor 4A-II OR Eukaryotic translation initiation factor 4A1	Q5VLR5 AND Q5RKI1 OR Q6P3V8	GO:0006457 protein folding GO:0006950 response to stress GO:0006986 response to unfolded protein GO:0009100 glycoprotein metabolic process GO:0045454 cell redox homeostasis AND GO:0006413 translational initiation

3509	Eukaryotic translation initiation factor 4A1	Q6P3V8	GO:0006413 translational initiation
4009	Fatty acid-binding protein	P07483	GO:0006631 fatty acid metabolic process GO:0006635 fatty acid beta-oxidation GO:0006656 phosphatidylcholine biosynthetic process GO:0006810 transport GO:0015909 long-chain fatty acid transport GO:0032868 response to insulin stimulus GO:0042493 response to drug GO:0070542 response to fatty acid
5001	Adenine phosphoribosyltransferase	P36972	GO:0006166 purine ribonucleoside salvage GO:0006168 adenine salvage GO:0007595 lactation GO:0009116 nucleoside metabolic process GO:0032869 cellular response to insulin stimulus
6001	Co lin-1	P45592	GO:0006606 protein import into nucleus GO:0007010 cytoskeleton organization GO:0022604 regulation of cell morphogenesis GO:0030030 cell projection organization GO:0045792 negative regulation of cell size
6516	Elongation factor 1-gamma	Q68FR6	GO:0006412 translation GO:0006414 translational elongation
4727 5702 5710 5716 6601	Protein disul de-isomerase A3	P11598	GO:0006662 glycerol ether metabolic process GO:0043065 positive regulation of apoptotic process GO:0045454 cell redox homeostasis
4810 4818	Alpha-fetoprotein	P02773	GO:0001542 ovulation from ovarian follicle GO:0001889 liver development GO:0006810 transport GO:0010033 response to organic substance GO:0019953 sexual reproduction GO:0031016 pancreas development GO:0031100 organ regeneration GO:0042448 progesterone metabolic process GO:0060395 SMAD protein signal transduction
4832 5805 6802	Serum albumin	P02770	GO:0006810 transport GO:0006950 response to stress GO:0007584 response to nutrient GO:0009267 cellular response to starvation GO:0010033 response to organic substance GO:0019836 hemolysis by symbiont of host erythrocytes GO:0042311 vasodilation GO:0043066 negative regulation of apoptotic process GO:0046010 positive regulation of circadian sleep/wake cycle, non-REM sleep GO:0046689 response to mercury ion GO:0051659 maintenance of mitochondrion location GO:0070541 response to platinum ion

SSP 2512 contained two proteins.

Table 4. KEGG pathway mapping of proteins identi ed by two-dimensional electrophoresis analysis of rat embryos cultured in the presence of ethanol

Pathway ID	Pathway name	UniProtKB AC	Protein Name (Total number of mapped pathways)
rno04612	Antigen processing and presentation	P06761	78 kDa glucose-regulated protein (4)
		P11598	Protein disul de-isomerase A3 (2)
		P63018	Heat shock cognate 71 kDa protein (9)
rno04141	Protein processing in endoplasmic reticulum	P06761	78 kDa glucose-regulated protein (4)
		P11598	Protein disul de-isomerase A3 (2)
		P63018	Heat shock cognate 71 kDa protein (9)
rno05134	Legionellosis	P63018	Heat shock cognate 71 kDa protein (9)
		Q68FR6	Elongation factor 1-gamma (1)
rno03040	Spliceosome	P63018	Heat shock cognate 71 kDa protein (9)
rno04010	MAPK signaling pathway	P63018	Heat shock cognate 71 kDa protein (9)
rno04144	Endocytosis	P63018	Heat shock cognate 71 kDa protein (9)
rno05145	Toxoplasmosis	P63018	Heat shock cognate 71 kDa protein (9)
rno05162	Measles	P63018	Heat shock cognate 71 kDa protein (9)
rno05164	In uenza A	P63018	Heat shock cognate 71 kDa protein (9)
rno04360	Axon guidance	P45592	Co lin-1 (4)
rno04666	Fc gamma R-mediated phagocytosis	P45592	Co lin-1 (4)
rno04810	Regulation of actin cytoskeleton	P45592	Co lin-1 (4)
rno05133	Pertussis	P45592	Co lin-1 (4)
rno04260	Cardiac muscle contraction	P16409	Myosin light chain 3 (3)
rno05410	Hypertrophic cardiomyopathy (HCM)	P16409	Myosin light chain 3 (3)
rno05414	Dilated cardiomyopathy	P16409	Myosin light chain 3 (3)
rno00230	Purine metabolism	P36972	Adenine phosphoribosyltransferase (2)
rno01100	Metabolic pathways	P36972	Adenine phosphoribosyltransferase (2)
rno03060	Protein export	P06761	78 kDa glucose-regulated protein (4)
rno05020	Prion diseases	P06761	78 kDa glucose-regulated protein (4)
rno03013	RNA transport	Q5RKI1	Eukaryotic initiation factor 4A-II (1)
		OR	OR
		Q6P3V8	Eukaryotic translation initiation factor 4A1 (1)
rno03320	PPAR signaling pathway	P07483	Fatty acid-binding protein (1)

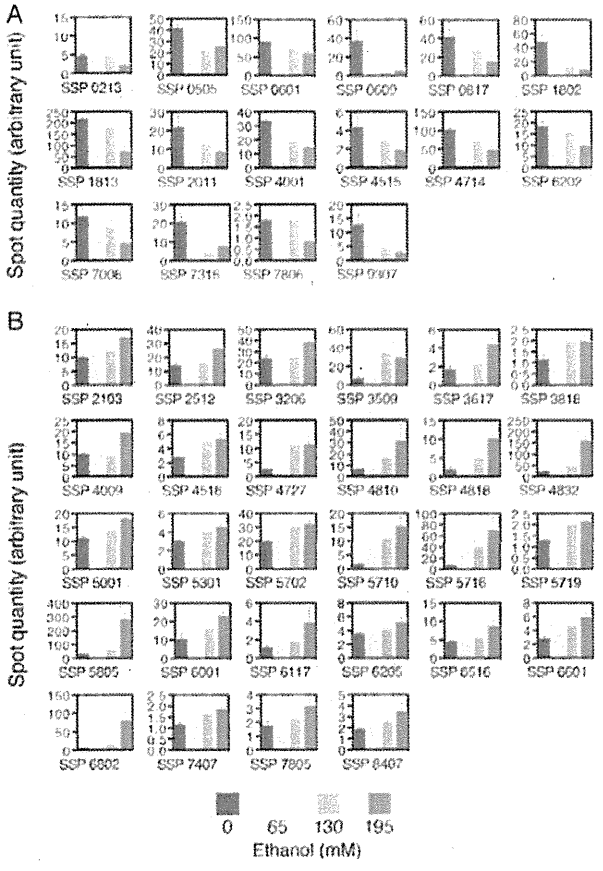

Fig. 3. Quanti cation of protein spots with expression changes in two-dimensional electrophoresis gels from rat embryos cultured in the presence of ethanol. Intensities of protein spots with ethanol-induced expression changes are shown. A. Protein spots with decreased intensity. B. Protein spots with increased intensity. Error bars indicate the standard error of the mean.

tein (standard spot numbers (SSPs) 4810, 4818), co lin-1 (SSP 6001), and serum albumin (SSPs 4832, 5805, 6802), were the same as those identi ed as candidate proteins involved in embryotoxicity in our previous studies (Usami *et al.*, 2009, 2008); co lin-1, which was increased, was found to be in its phosphorylated form.

Several protein spots were identified as charge variant forms of the same proteins, i.e., protein disul de isomerase A3 (PDIA3; SSPs 4714, 4727, 5702, 5710, 5716, 6601), alpha-fetoprotein (SSPs 4810, 4818), and serum albumin (SSPs 4832, 5805, 6802). The quantities of spots that were identi ed as PDIA3 were increased (SSPs 4727, 5702, 5710, 5716, 6601), as well as decreased (SSP 4714) (Fig. 3). Because the PDIA3 spot with decreased quantity was the most acidic spot, it appeared that a basic pI shift of PDIA3 occurred in the groups exposed to ethanol.

Classification and mapping of proteins with ethanol-induced expression changes

According to their GO terms, the identified proteins were classified into various categories; the six major categories were "metabolism" (including 32% of the GO terms), "protein metabolism" (13%), "death" (9%), "developmental processes" (9%), "cell organization and biogenesis" (8%), and "stress response" (8%).

The identi ed proteins were mapped to 22 pathways using the KEGG pathway mapper (Table 4). Multiple proteins, i.e., PDIA3, 78-kDa glucose-regulated protein (SSP 1802), and heat shock cognate 71-kDa protein (SSP 1813), were mapped to the same two pathways, i.e., "protein processing in endoplasmic reticulum" (rno04141) and "antigen processing and presentation" (rno04612). Some proteins were mapped to multiple pathways, e.g., heat shock cognate 71-kDa protein (nine pathways), 78-kDa glucose-regulated protein (four pathways), and co lin-1 (four pathways).

DISCUSSION

As mechanisms of ethanol-induced embryotoxicity, oxidative stress, and inhibited retinoid synthesis have been proposed (Goodlett *et al.*, 2005), which seems to be in accordance with the GO classi cation (32% metabolism and 8% stress response) of the proteins identi ed in the present study. In this context, expression changes in PDIA3 (also known as GRp58 and ERp57) are intriguing because it is an endoplasmic reticulum stress protein with oxidoreductase activity that regulates cellular redox homeostasis (Frickel *et al.*, 2004; Ni and Lee, 2007). PDIA3 is also involved in the nuclear translocation of retinoic acid receptor alpha (Zhu *et al.*, 2010) and its de ciency is embryonic lethal (Coe *et al.*, 2010). The identi ed proteins with GO terms classi ed into "death" may be involved in ethanol-induced apoptosis of neuronal cells, which has frequently been observed (Ahlgren *et al.*, 2002; Giles *et al.*, 2008). The present results also agreed with some biological networks that were perturbed by ethanol in cultured whole mouse embryos, involving cell death, reproductive system and antigen processing (Mason *et al.*, 2012). The pathways associated with multiple identi ed proteins may be more susceptible to ethanol, because these pathways could be affected at multiple steps simultaneously. On the other hand, the nding that

multiple pathways were associated with the same proteins might partially explain the complexity of ethanol-induced embryotoxicity.

ACKNOWLEDGMENT

This work was supported by a Health and Labor Science Research Grant from the Ministry of Health, Labor and Welfare in Japan.

REFERENCES

Ahlgren, S.C., Thakur, V. and Bronner-Fraser, M. (2002): Sonic hedgehog rescues cranial neural crest from cell death induced by ethanol exposure. Proc. Natl. Acad. Sci. USA, **99**, 10476-10481.

Chen, H., Boontheung, P., Loo, R.R., Xie, Y., Loo, J.A., Rao, J.Y. and Collins, M.D. (2008): Proteomic analysis to characterize differential mouse strain sensitivity to cadmium-induced forelimb teratogenesis. Birth Defects Res. A Clin. Mol. Teratol., **82**, 187-199.

Coe, H., Jung, J., Groenendyk, J., Prins, D. and Michalak, M. (2010): ERp57 modulates STAT3 signaling from the lumen of the endoplasmic reticulum. J. Biol. Chem., **285**, 6725-6738.

Frickel, E.-M., Frei, P., Bouvier, M., Stafford, W.F., Helenius, A., Glockshuber, R. and Ellgaard, L. (2004): ERp57 is a multifunctional thiol-disul de oxidoreductase. J. Biol. Chem., **279**, 18277-18287.

Giavini, E., Broccia, M.L., Prati, M., Bellomo, D. and Menegola, E. (1992): Effects of ethanol and acetaldehyde on rat embryos developing *in vitro*. Vitr. Cell. Dev. Biol., **28A**, 205-210.

Giles, S., Boehm, P., Brogan, C. and Bannigan, J. (2008): The effects of ethanol on CNS development in the chick embryo. Reprod. Toxicol., **25**, 224-230.

Goodlett, C.R., Horn, K.H. and Zhou, F.C. (2005): Alcohol teratogenesis: mechanisms of damage and strategies for intervention. Exp. Biol. Med., **230**, 394-406.

Groebe, K., Hayess, K., Klemm-Manns, M., Schwall, G., Wozny, W., Steemans, M., Peters, A.K., Sastri, C., Jaeckel, P., Stegmann, W., Zengerling, H., Schopf, R., Poznanovic, S., Stummann, T.C., Seiler, A., Spielmann, H. and Schrattenholz, A. (2010): Protein biomarkers for *in vitro* testing of embryotoxicity. J. Proteome Res., **9**, 5727-5738.

Hu, Z.-L., Bao, J. and Reecy, J.M. (2008): CateGOrizer: A web-based program to batch analyze gene ontology classi cation categories. Online J. Bioinforma., **9**, 108-112.

Jain, E., Bairoch, A., Duvaud, S., Phan, I., Redaschi, N., Suzek, B.E., Martin, M.J., McGarvey, P. and Gasteiger, E. (2009): Infrastructure for the life sciences: design and implementation of the UniProt website. BMC Bioinformatics, **10**, 136.

Li, H. and Kim, K.H. (2003): Effects of ethanol on embryonic and neonatal rat testes in organ cultures. J. Androl., **24**, 653-660.

Mason, S., Anthony, B., Lai, X., Ringham, H.N., Wang, M., Witzmann, F.A., You, J.-S. and Zhou, F.C. (2012): Ethanol exposure alters protein expression in a mouse model of fetal alcohol spectrum disorders. Int. J. Proteomics, **2012**, 867141.

Ni, M. and Lee, A.S. (2007): ER chaperones in mammalian development and human diseases. FEBS Lett., **581**, 3641-3651.

Szabo, G., Puppolo, M., Verma, B. and Catalano, D. (1994): Regulatory potential of ethanol and retinoic acid on human monocyte functions. Alcohol. Clin. Exp. Res., **18**, 548-554.

UniProt Consortium (2011): Ongoing and future developments at the Universal Protein Resource. Nucleic Acids Res., **39**, D214-219.

Usami, M. and Mitsunaga, K. (2011): Proteomic analysis and *in vitro* developmental toxicity tests for mechanism-based safety evaluation of chemicals. Expert Rev. Proteomics, **8**, 153-155.

Usami, M., Mitsunaga, K., Nakazawa, K. and Doi, O. (2008): Proteomic analysis of selenium embryotoxicity in cultured postimplantation rat embryos. Birth Defects Res. B Dev. Reprod. Toxicol., **83**, 80-96.

Usami, M., Nakajima, M., Mitsunaga, K., Miyajima, A., Sunouchi, M. and Doi, O. (2009): Proteomic analysis of indium embryotoxicity in cultured postimplantation rat embryos. Reprod. Toxicol., **28**, 477-488.

Wentzel, P. and Eriksson, U.J. (2008): Genetic in uence on dysmorphogenesis in embryos from different rat strains exposed to ethanol *in vivo* and *in vitro*. Alcohol. Clin. Exp. Res., **32**, 874-887.

Zhou, F.C., Zhao, Q., Liu, Y., Goodlett, C.R., Liang, T., McClintick, J.N., Edenberg, H.J. and Li, L. (2011): Alteration of gene expression by alcohol exposure at early neurulation. BMC Genomics, **12**, 124.

Zhu, L., Santos, N.C. and Kim, K.H. (2010): Disul de isomerase glucose-regulated protein 58 is required for the nuclear localization and degradation of retinoic acid receptor alpha. Reproduction, **139**, 717-731.

Congenital Anomalies
THE JAPANESE TERATOLOGY SOCIETY
doi:10.1111/cga.12036
Congenital Anomalies 2014; **54**, 67–68

LETTER TO THE EDITOR

Various definitions of reproductive indices: A proposal for combined use of brief definitions

Makoto Usami[1], Katsuyoshi Mitsunaga[2], Tomohiko Irie[1], and Mikio Nakajima[3]
[1]Division of Pharmacology, National Institute of Health Sciences, Tokyo, [2]School of Pharmaceutical Sciences, Toho University, Chiba, and [3]Pharmaceuticals Research Center, Asahi Kasei Pharma Corporation, Shizuoka, Japan

Several reproductive indices, such as live birth index, are calculated as endpoints to be evaluated in toxicity tests concerning reproductive effects of chemicals. These indices are useful to correct for variations resulting from infertility and multiple pregnancy, for example, the varied numbers of pups, among treatment groups and dams, respectively. In the toxicity test reports, the reproductive indices are used with their definitions, usually expressed as calculation formulae, to describe what they mean.

Despite their frequent use, however, the definitions of the reproductive indices have not been standardized; that is, they are different among laboratories, and are confusing. For example, the live birth index is "number of live newborns/number of implantation sites × 100" in some laboratories, but is "number of live newborns/number of total newborns × 100" in others, as listed in Table 1. These two definitions are quite different from each other in that the latter does not involve postimplantation loss, but the former does, though the live birth index is one of the most important reproductive indices. In most toxicity test laboratories, on the other hand, the definitions of reproductive indices cannot be changed even for standardization because they are defined as a part of laboratory computer systems.

In the database era, the confusion of reproductive indices has become more serious than ever, because data from various laboratories in the toxicity databases are frequently consulted at a time as in meta-analyses for building quantitative structure-activity relationship models. In the meta-analysis of reproductive toxicity data, reproductive indices cannot be used as toxicological endpoints to be evaluated unless their definitions, usually not found in the abstract because of their lengthiness, are clearly identified.

As a solution to this issue, we here propose combined use of brief definitions that describe the meaning of the reproductive indices with simpler words than the calculation formulae, for example, "live newborn/nidation rate" for "number of live newborns/number of implantation sites × 100." Explanatory descriptions of the reproductive indices with their brief definitions, for example, "the live birth index (live newborn/nidation rate)" at their first appearance in the abstract and main text would be most helpful.

In this letter, we show various definitions of representative reproductive indices and propose their brief definitions. We found 14 reproductive indices with 23 definitions by a brief survey of toxicological reference books (Manson and Kang 1989; Mizutani 1992; Saikikeisei ni kansuru dejitaruka sagyogruupu iinkai 1994; Econbichon 1995; Parker 2012) and contract research organizations' reports in a toxicological database (Japan Existing Chemical Data Base, http://dra4.nihs.go.jp/mhlw_data/jsp/SearchPage.jsp). From these indices, we show seven representative indices and 12 brief definitions as examples (Table 1), but it is not intended that the brief definitions presented here should be used as they are.

Correspondence: Makoto Usami, PhD, Division of Pharmacology, National Institute of Health Sciences, 1-18-1, Setagaya, Tokyo 158-8501, Japan. Email: usami@nihs.go.jp
Received August 28, 2013; revised and accepted October 29, 2013.

REFERENCES

Econbichon DJ. 1995. Reproductive toxicology. In: Derelanko MJ, Hollinger MA, editors. CRC handbook of toxicology. Boca Raton: CRC Press. p 379–402.

Manson JM, Kang YJ. 1989. Test methods for assessing female reproductive and developmental toxicology. In: Hayes AW, editor. Principles and methods of toxicology, 2nd edn. New York: Raven Press, Ltd. p 311–359.

Mizutani M. 1992. Seisyoku hassei dokusei no jissai. In: Tanimura T, editor. Developmental toxicology. Tokyo: Chijinshokan. p 143–167. (In Japanese.)

Parker RM. 2012. Reproductive toxicity testing-Methodology. In: Hood RD, editor. Developmental and reproductive toxicology: a practical approach, 3rd edn. London: Informa Healthcare. p 184–228.

Saikikeisei ni kansuru dejitaruka sagyogruupu iinkai. 1994. Saikikesei Yogo. In: Nakadate M, editor. Toxicity testing. Tokyo: National Institute of Health Sciences, Biological Safety Research Center. p 394–488. (In Japanese.) Available at URL: http://www.nihs.go.jp/center/yougo/saiki.html.

Table 1 Representative reproductive indices and their definitions appeared in reference books and toxicity reports

Reproductive index	Definition†									Example of brief definition
	Reference Book					Contract research organization's reproductive toxicity test report				
	Manson & Kang, 1989	Mizutani, 1992	Ecobichon, 1995	Saikikeisei, 1994	Parker, 2012	Laboratory A	Laboratory B	Laboratory C	Laboratory D	
Implantation index					Implants/Corpora lutea	Implantation sites/ Corpora lutea	Implantation sites/ Corpora lutea	Implantation scars/ Corpora lutea	Implantation sites/ Corpora lutea	Nidation/luteum rate
			Implantations/Pregnant females							Nidation/pregnant rate
Gestation index		Females with live offspring/Pregnant females		Females with live offspring/Pregnant females	Females with live born/Females with evidence of pregnancy	Females with live pups/ Pregnant females				Live delivered dam/pregnant rate
Delivery index							Females which delivered live borns/ Pregnant females	Dams with live offspring/Pregnant dams	Pregnant females with live pups at birth/ Pregnant females	
		Pups born/Implantation sites				Pups born/Implantation sites		Offspring at birth/ Implantation scars	Pups born/Implantation sites	Newborn/nidation rate
Live birth index			(Viable pups born/ litter)/(Pups born/ litter)		Pups born alive/Total pups born	Live pups on lactation day 0/Pups born		Live offspring at birth/ Offspring at birth	Live pups at birth/Pups born	Live/total newborn rate
	Pups alive day 1/Pups born alive									Day 1 live pup/live newborn rate
		Live born/Implantation sites					Live born/Implantation sites			Live newborn/ nidation rate
Birth index				Offspring born alive/ Implantations				*Live offspring at birth/* Implantation scars	*Live pups at birth/* Implantation sites	
Viability index		Offspring alive on day 4 after birth/Live born		Offspring alive on day 4 after birth/Offspring born alive		Live pups on lactation day 4/Live pups on lactation day 0	Live pups on postnatal day 4/Live born	Live offspring at 4 days after birth/Live offsprings at birth	Live pups on postnatal day 4/Live pups at birth	Day 4 live pup/live newborn rate
	Pups alive day 7/Pups alive *day 1*									Days x/y live/live pup rate
			Viable pups born/Dead pups born							Live/dead newborn rate
Sex ratio (at birth)			Male offspring/Female offspring		Male offspring/Total offspring	Male pups born/Pups born		Male offspring/(Male offspring + female offspring)	Males born/Pups born	Male/total pup rate
						Live male pups/Live pups	Live born males/Live born			Live male /live total pup rate

†Common descriptions, "number of" and "× 100," are omitted.

Development/Plasticity/Repair

Microglia Enhance Neurogenesis and Oligodendrogenesis in the Early Postnatal Subventricular Zone

Yukari Shigemoto-Mogami,[1] Kazue Hoshikawa,[1] James E. Goldman,[2] Yuko Sekino,[1] and Kaoru Sato[1]

[1]Laboratory of Neuropharmacology, Division of Pharmacology, National Institute of Health Sciences, Tokyo 158-8501, Japan, and [2]Department of Pathology and Cell Biology, Columbia University College of Physicians and Surgeons, New York, New York 10032

Although microglia have long been considered as brain resident immune cells, increasing evidence suggests that they also have physiological roles in the development of the normal CNS. In this study, we found large numbers of activated microglia in the forebrain subventricular zone (SVZ) of the rat from P1 to P10. Pharmacological suppression of the activation, which produces a decrease in levels of a number of proinflammatory cytokines (i.e., IL-1β, IL-6, TNF-α, and IFN-γ) significantly inhibited neurogenesis and oligodendrogenesis in the SVZ. *In vitro* neurosphere assays reproduced the enhancement of neurogenesis and oligodendrogenesis by activated microglia and showed that the cytokines revealed the effects complementarily. These results suggest that activated microglia accumulate in the early postnatal SVZ and that they enhance neurogenesis and oligodendrogenesis via released cytokines.

Key words: cytokine; microglia; neurogenesis; neurosphere; oligodendrogenesis; subventricular zone

Introduction

CNS microglia have long been considered as resident immune cells, which are activated in response to pathological events. In pathological conditions, they change their morphology to an amoeboid shape, acquiring activation-specific phenotypes, such as chemotaxis, phagocytosis, and secretion of inflammatory cytokines (Nakajima and Kohsaka, 2001; Inoue, 2008; Monji et al., 2009; Kettenmann et al., 2011). However, microglia also have physiological roles in the normal CNS. They actively survey their territory with fine processes and receive stimuli from the environment as sensor cells (Kettenmann et al., 2011). *In vivo* lineage tracing studies have established that microglia differentiate from primitive myeloid progenitors that arise before embryonic day 8 and are identified in the CNS parenchyma even before definitive hematopoiesis (Ginhoux et al., 2010), whereas it has also been shown that microglia migrate from the lateral ventricle into the brain via the subventricular zone (SVZ) in the postnatal brain (Mohri et al., 2003). In the early embryonic brain, most microglia adopt an amoeboid morphology and characteristics of an activated form (Hirasawa et al., 2005). Microglia in the embryonic SVZ limit the production of cortical neurons by phagocytosing neural precursor cells (Cunningham et al., 2013). The number of microglia in the brain reaches a maximum during the early postnatal weeks (Wu et al., 1993; Xu and Ling, 1994), after which they transform into cells with a ramified shape, the typical morphology observed in the adult CNS (Ignácio et al., 2005). However, microglia are densely populated in neurogenic niches, such as the SVZ (Mosher et al., 2012), and appear more activated in the adult SVZ than in non-neurogenic zones (Goings et al., 2006). These developmental changes in the activation and the distribution of microglia strongly suggest that microglia play important roles in CNS development. However, the developmental dynamics of microglia in the postnatal SVZ and their roles in neurogenesis and gliogenesis at this stage are not well understood. We have examined the distribution and morphology of microglia in the rat forebrain during the neonatal-early postnatal period in detail and found a large number of active forms within the SVZ from P1 to P10, which then transformed from an activated form to a ramified form after P14. We here present evidence that microglia in the early postnatal SVZ promote both neurogenesis and oligodendrogenesis and that cytokines are important in these effects. To our knowledge, this is the first report showing a novel physiological function of microglia regulating neurogenesis and oligodendrogenesis in the early postnatal brain.

Received April 15, 2013; revised Dec. 21, 2013; accepted Dec. 27, 2013.

Author contributions: K.S. designed research; Y.S.-M., K.H., and K.S. performed research; Y.S.-M., K.H., J.E.G., Y.S., and K.S. analyzed data; Y.S.-M., J.E.G., Y.S., and K.S. wrote the paper.

This work was supported in part by a Grant-in-Aid for Young Scientists from MEXT, Japan (KAKENHI 21700422), the Program for Promotion of Fundamental Studies in Health Sciences of NIBIO, Japan, a Health and Labor Science Research Grant for Research on Risks of Chemicals, a Labor Science Research Grant for Research on New Drug Development from the MHLW, Japan to K.S., and a Health and Labor Science Research Grant for Research on Publicly Essential Drugs and Medical Devices, Japan to Y.S.

The authors declare no competing financial interests.

This article is freely available online through the *J Neurosci* Author Open Choice option.

Correspondence should be addressed to Dr. Kaoru Sato, Laboratory of Neuropharmacology, Division of Pharmacology, National Institute of Health Sciences, Kamiyoga 1-18-1, Setagaya-ku, Tokyo 158-8501, Japan. E-mail: kasato@nihs.go.jp.

DOI:10.1523/JNEUROSCI.1619-13.2014

 0270-6474/14/342231-13$15.00/0

Materials and Methods

Animals and treatment. All animals were treated in accordance with the guidelines for the Care and Use of Laboratory Animals of the Animal Research Committee of the National Institute of Health Sciences and followed the *Guide for the Care and Use of Laboratory Animals*. All experiments were approved by the Animal Research Committee of National Institute of Health Sciences and conformed to the relevant regulatory standards. The Wistar rats were purchased from Japan SLC and maintained under specific pathogen-free conditions at a controlled temperature and humidity and on a 12 h light/12 h dark cycle and had *ad libitum*

2232 • J. Neurosci., February 5, 2014 • 34(6):2231–2243

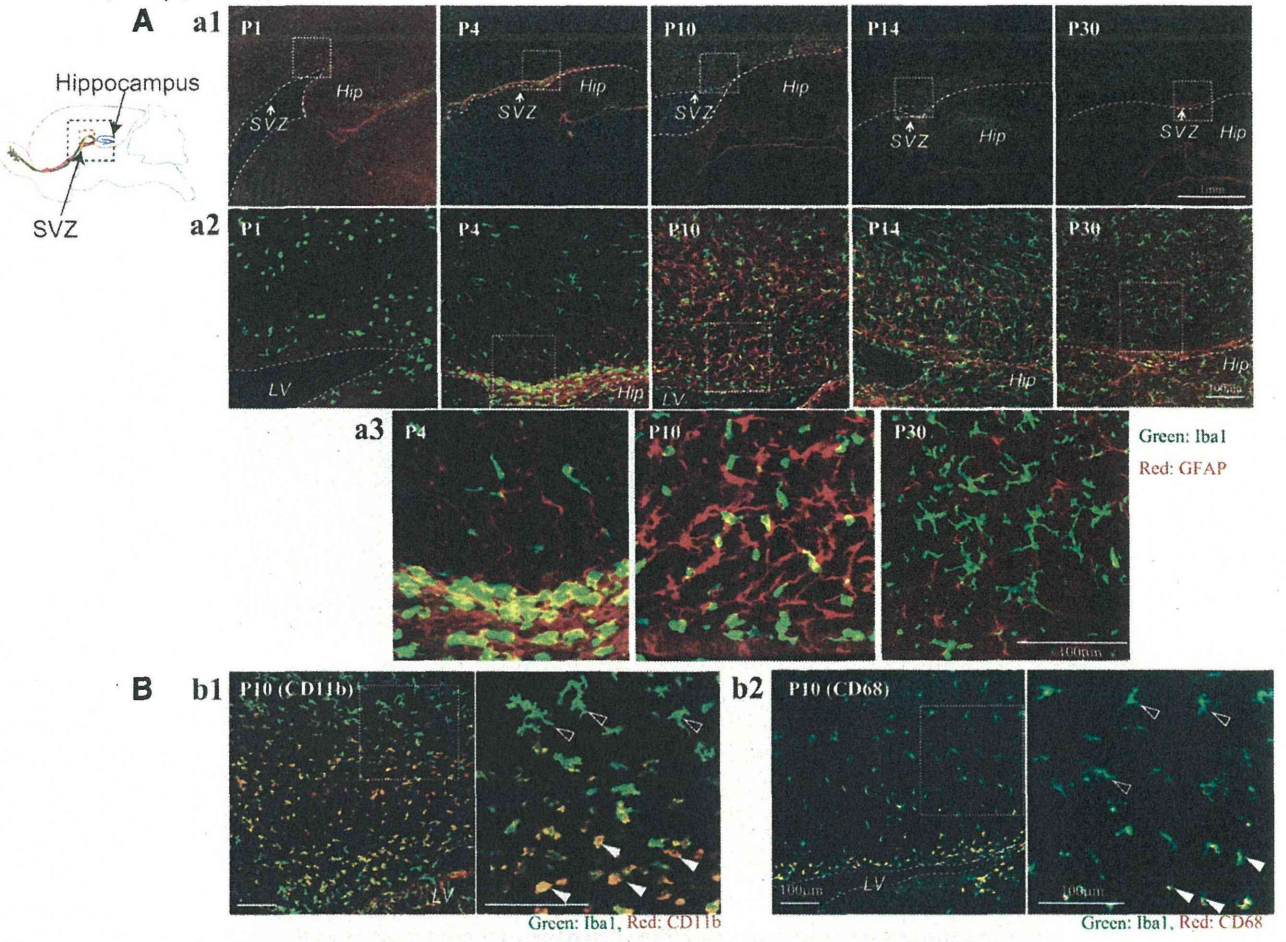

Figure 1. There is a population of activated microglia accumulated in the early postnatal SVZ. ***Aa1***, Distribution of microglia in the postnatal VZ/SVZ (P1, P4, P10, P14, P30). Sagittal sections of forebrains were immunostained with anti-Iba1 (green: microglia) and anti-GFAP antibodies (red: neural stem cells and astrocytes). ***Aa2***, Magnified images of the hatched squares in ***Aa1***. The accumulation in the SVZ in P4 and P10 was distinctive. ***Aa3***, Magnified images of the hatched squares in ***Aa2***. Morphological changes of microglia with age from amoeboid shape to more ramified shape is remarkable (P4, P10, P30). ***Bb1***, Activation of microglia in P10 SVZ. Sagittal sections immunostained with anti-CD11b (red: activated microglia) and anti-Iba1 antibodies (green: microglia). Right panel, Magnified image of the hatched square in the left panel. The microglia in the SVZ have an amoeboid shape and positive for CD11b (white arrowheads), whereas those outside SVZ have more ramified shape and are negative for CD11b (black arrowheads). ***Bb2***, Sagittal sections immunostained with anti-CD68 (red: activated microglia) and anti-Iba1 antibodies (green: microglia). Right panel, Magnified image of the hatched square in the left panel. The microglia in the SVZ have an amoeboid shape and positive for CD68 (white arrowheads), whereas those outside SVZ have more ramified shape and are negative for CD68 (black arrowheads). Similar results were obtained in three independent experiments.

access to food and water. Minocycline (30 mg/kg) or the same volume of PBS was injected into rats of either sex intraperitoneally for 3 d from postnatal day 2 (P2). Six hours after the last injection, rats were deeply anesthetized and the brains were removed on ice.

Immunohistochemistry (sagittal sections). Rats (P1, P4, P10, P14, P30) were anesthetized and then perfused with saline followed by 4% PFA, and then the brains were removed. From each half brain, sagittal sections were cut laterally at a thickness of 30 μm beginning 2 mm lateral from the midline. The sections were incubated for 2 h at room temperature in a blocking solution (3% normal goat serum, 0.3% Triton X-100 in PBS) and incubated for 24 h at 4°C in the solution, including the primary antibodies (rabbit anti-Iba1 antibody [019–9741, Wako; 1:500], mouse anti-GFAP antibody [MAB3402, Millipore; 1:200], mouse anti-rat CD11b antibody [MAB1405, AbD Serotec; 1:100], anti-rat CD68 antibody [MCA341R, AbD Serotec; 1:100], rabbit anti-Ki-67 [SP6, M3061, Spring Bioscience; 1:10], anti-nestin antibody [MAB353, Millipore; 1:100], goat anti-doublecortin [Dcx] antibody [sc-8066, Santa Cruz Biotechnology; 1:200], goat anti-PDGFRα antibody [sc-31178, Santa Cruz Biotechnology; 1:50], anti-oligodendrocyte marker O1 [O1] antibody [MAB344, Millipore, 1:50], mouse anti-MBP antibody [MAB 382, Millipore; 1:50], rabbit anti-ALDH1L1 antibody-astrocyte marker antibody [ab87117, Abcam; 1:1000], mouse anti-S100β antibody [S2532, Sigma; 1:100], rabbit anti IGF-1 antiserum [GroPep Biotechnology; [1:200]) After incubation, the sections were washed and incubated for 3 h at room temperature in the solution, including the secondary antibodies (anti-rabbit IgG-conjugated Alexa Fluorochrome or anti-mouse IgG-conjugated Alexa Fluorochrome [Invitrogen; 1:1000]). The stained sections were analyzed using a Nikon A1R-A1 confocal microscope system. To count the number of cells positive for each differentiation marker, 613 × 613 μm^2 and 1024 × 1024 μm^2 squares were set on both sides of the fornix. The cell numbers in the two squares were counted and averaged for the cell numbers in one section. The averaged data of 3 sections at 90 μm intervals were treated as the data of one animal and the data from 6 animals were statistically analyzed.

Immunohistochemistry (coronal sections). Three points on the skull at three different rostrocaudal stereotaxic coordinates (i.e., anterior, middle, posterior) were marked with animal tattoo ink (Ketchum) at P1. These three points with different rostrocaudal levels were determined according to a previous report (Suzuki and Goldman, 2003): rostral point: 2 mm anterior, 1 mm lateral to the bregma; middle point: 0.7 mm anterior, 1 mm lateral to the bregma; caudal point: 0.5 mm posterior, 1 mm lateral to the bregma. Then the animals were perfused at P1, P3, P10, and P30, and the brains were removed as described above. From each half brain, coronal sections were cut at each marked point from anterior to posterior. The sections were immunostained with anti-Iba1 and anti-CD68 as described above. After immunostaining, the sections were coun-

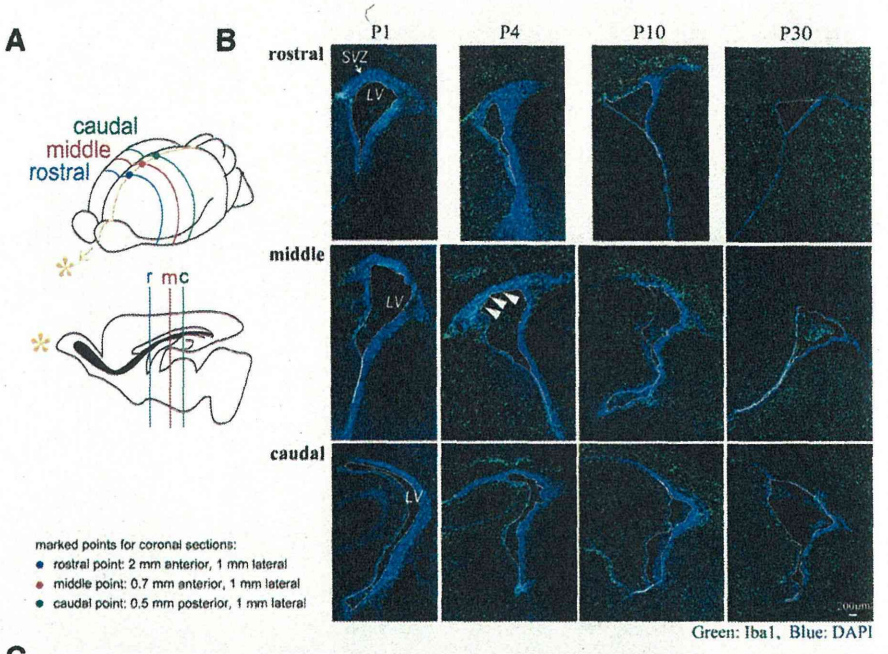
A
B
caudal
middle
rostral
r mc
P1
P4
P10
P30
rostral
middle
caudal
SVZ
LV
marked points for coronal sections:
rostral point: 2 mm anterior, 1 mm lateral
middle point: 0.7 mm anterior, 1 mm lateral
caudal point: 0.5 mm posterior, 1 mm lateral
Green: Iba1, Blue: DAPI

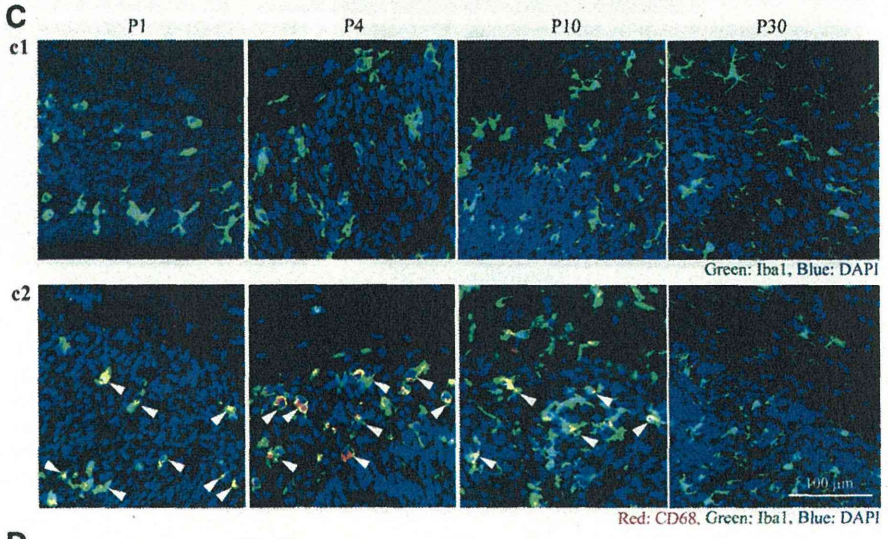
C
c1
c2
P1
P4
P10
P30
Green: Iba1, Blue: DAPI
100 μm
Red: CD68, Green: Iba1, Blue: DAPI

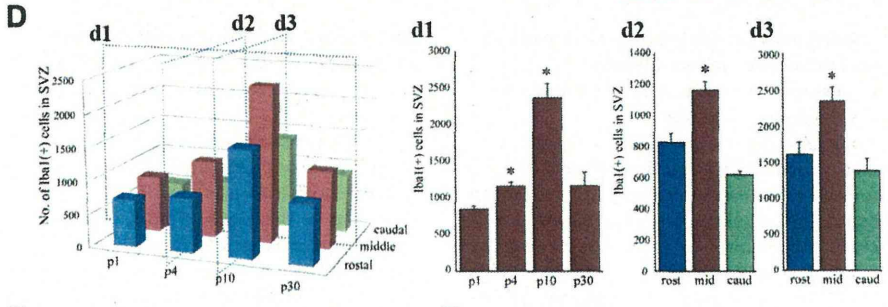
D
d1
d2
d3
No. of Iba1(+) cells in SVZ
caudal
middle
rostral
p1
p4
p10
p30
Iba1(+) cells in SVZ
rost
mid
caud

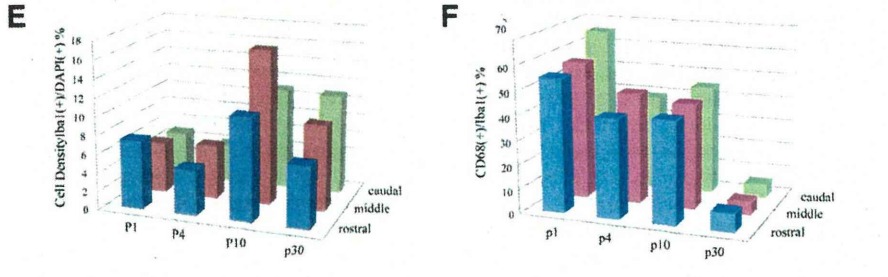
E
F
Cell Density(Iba1(+)/DAPI(+)) %
CD68(+)/Iba1(+) %
caudal
middle
rostral
p1
p4
p10
p30

terstained with DAPI (1:500; Invitrogen) for 30 min to visualize the SVZ. The cell numbers of microglia (Iba1$^+$) and activated microglia (Iba1$^+$ CD68$^+$) in the SVZ (the region with dense DAPI signals) were counted in one section. The averaged data of three sections at 90 μm intervals across the marked points were treated as the data for each rostrocaudal level. The data from 6 to 9 hemispheres per one rostrocaudal level were statistically analyzed.

Western blotting. P4 Wistar rat brains were cut into sagittal sections. Under a microscope, a parasagittal section (from 1 mm lateral, 2 mm thickness) was taken from each half brain and meninges were carefully removed. The VZ/SVZ was identified by its slightly darker, more transparent appearance compared with the overlying corpus callosum. We cut out the VZ/SVZ between 0.4 mm anterior and 3 mm posterior (posterior end of SVZ) from bregma so as not to include the rostral migratory stream. Dissected VZ/SVZ tissues were homogenized on ice in extraction buffer (20 mM Tris, 2 mM EDTA, 0.5 mM EGTA, 0.32 M sucrose, protease inhibitor mixture), and centrifuged at 1000 × *g* for 10 min. Proteins in the lysates were resolved with SDS-PAGE and transferred to PVDF membranes. The membranes were incubated overnight in BlockAce blocking solution at 4°C. Then the membranes were incubated with primary antibodies (anti-CD11b [1:1000], anti-CD68 [1:2000], anti-nestin [1:1000], anti-PDGFRα [1:200], anti-ALDH1L1 [1:1000], anti-S100β [1:2000]) for 1 h at 25°C. After washing three times, the membranes were incubated with HRP-conjugated anti-rabbit or anti-mouse antibody (1:5000) for 1 h at 25°C. The membranes were then washed three times and signals were visualized by chemiluminescence detectors LAS3000 (Fuji film).

Measurement of cytokine levels. Cytokine levels in the SVZ were determined with Bio-Plex cytokine analysis system (Bio-Rad Laboratories). Tissue lysates of VZ/SVZ fractions were obtained from rats at P1, P4, P10, and P30 as described in Western blotting. The concentrations of Il-1α, Il-1β, IL-2, IL-4, IL-6, Il-10, GM-CSF, IFN-γ, and TNF-α were measured by the Bio-Plex rat cytokine 9 plex kit according to the manufacturer's instruction. In some cases, IGF-1, Il-1β IL-6, TNF-α, and IFN-γ concentrations were measured by ELISA kit according to the manufacturer's instruction. The protein levels of tissue lysates were measured by BCA protein assay. The amount of each cytokine in 100 μg of total protein is shown for comparison. To determine the cytokine release from activated microglia *in vitro*, microglia were activated by LPS (10 ng/ml) in the presence or absence of minocycline (10 μM) for 30 min and washed carefully and incubated in the normal medium for 24 h. After 24 h incubation, the cell culture supernatants were collected, and concentration of Il-1β, IL-6, IFN-γ, and TNF-α were measured by ELISA kit.

Cell culture: neurosphere culture. Rat neural stem cells were cultured as previously described (Reynolds et al., 1992; Hamanoue et al., 2009) with slight modifications. Briefly, telencephalons were dissected from embryonic day 16 (E16) rats of either sex in ice-cold DMEM/F12, minced, and dispersed into single cells by pipetting. Cells were then cultured in DMEM/F12 containing B27 supplement (×200), 20 ng/ml FGF2, and 20 ng/ml EGF for 7 d. The primary neurospheres and single cells were differentiated in growth factor-free medium in glass chambers coated with ornithine/fibronectin. In some cases, primary neurosphere were incubated with TrypLE Select for 15 min and dissociated by pipetting. Single cells were differentiated in glass chambers coated with polyornithine/laminin.

Microglia culture. Rat microglia were cultured as previously described (Nakajima et al., 1992). In brief, mixed glial cultures were prepared from the cerebral cortex of P1 Wistar rats and maintained for 12–23 d in DMEM containing 10% FBS. The floating microglia over the mixed glial cultures were collected and transferred to appropriate dishes or transwells.

Neural stem cell differentiation assay. To examine the effects of activated microglia on neural development and the contribution of cytokines to the effects, we used modified cocultures of neurospheres with activated microglia. Microglia cultured independently of neurospheres on transwells were activated by LPS (10 ng/ml) in the presence or absence of minocycline (10 μM) for 30 min and washed carefully to prevent residual LPS and minocycline. The transwells on which microglia were cultured were set on the neurospheres 1 d after the starting point of the differentiation and incubated for differentiation periods suitable for neurons (7 d) or oligodendrocytes (11 d). In some cases, we performed the coculture of cells dissociated from neurospheres and activated microglia. To check the effects of minocycline alone, these cells were incubated in the presence of minocycline (10 μM) for 7 d. Neurospheres and single neural stem cells were immunohistochemically stained for β3-tubulin, PDGFRα, O4, GFAP, and TOTO3 according to the manufacture's instruction (Stem Cell Kits, R&D Systems). To examine the effects of function-blocking antibodies on differentiation, the neurospheres were differentiated in the presence of function-blocking antibodies (goat anti-rat IL-1β antibody [AF-501-NA, R&D Systems], goat anti-rat IL-6 antibody [AF-506, R&D Systems], TNF-α antibody [70R-TR007X, Fitzgerald], and goat anti-mouse/rat IFN-γ antibody [AF-585-NA, R&D Systems]) (1 μg/ml for each). The effects of these function-blocking antibodies were compared with the same concentration of isotype-matched control IgG: normal goat IgG control [AB-108-C, R&D Systems] and rabbit IgG control [31R-AR001, R&D Systems] (1 μg/ml for each). The effect of the mixture of function blocking antibodies (goat anti-rat IL-1β antibody, goat anti-rat IL-6 antibody, TNF-α antibody, and goat anti-mouse/rat IFN-γ antibody, 1 μg/ml for each) was compared with the control, which included same concentrations of isotype-matched control IgGs (i.e., 3 μg/ml of normal goat IgG control and 1 μg/ml of rabbit IgG control). To examine the effects of a single cytokine, the neurospheres were differentiated in the presence of each individual recombinant cytokine (rIL-1β, rIL-6, rTNF-α, and rIFN-γ at 1 or 10 ng/ml). After the differentiation period, the cells were stained immunocytochemically as described above.

Data analysis and statistics. All data are shown as the mean ± SEM. Statistical analysis was performed using Student's *t* test, or Tukey's test by ANOVA. Differences were considered to be significant at $p < 0.05$.

Materials. Minocycline, LPS, anti-S100β antibody (S2532), and EGF were purchased from Sigma. Bio-Plex rat cytokine 9 plex was purchased from Bio-Rad Laboratories. Recombinant cytokines (rIL-1β, rIL-4, rIL-6, rIFN-γ, rTNF-α) and FGF2 were purchased from PeproTech. Maximum sensitivity substrate and BCA protein assay were purchased from Thermo Scientific. CanGet Signals was purchased from Toyobo. HRP-conjugated anti-rabbit, mouse antibodies were purchased from GE Healthcare Life Science. DAPI, TOTO3, anti-mouse, sheep, rabbit IgG, and anti-mouse IgM-conjugated AlexaFluor were purchased from Invitrogen. BlockAce was purchased from DS Pharma Biomedical. B27 supplement, TrypLE Serect, FBS, and DMEM were purchased from Invitrogen.

Figure 2. The temporal and spatial dynamics of activated microglia in the postnatal SVZ. ***A***, A schematic of the rostrocaudal levels in this experiment. ***B***, The distribution of microglia in the rostral, medial, and caudal SVZ at P1, P4, P10, and P30. Coronal sections of forebrains at rostral (2 mm anterior to the bregma), medial (0.7 mm anterior to the bregma), and caudal (0.5 mm posterior to the bregma) levels were immunostained with anti-Iba1 (green: microglia) followed by DAPI staining (blue: cell nuclei). A population of activated microglia accumulated within the SVZ at P1-P10. ***Cc1***, Typical morphology of microglia in the middle SVZ at P1, P4, P10, and P30. Morphological change of microglia with age from amoeboid shape to more ramified shape is remarkable. ***Cc2***, The middle SVZ sections immunostained with anti-CD68 (red: activated microglia) and anti-Iba1 antibodies (green: microglia). The microglia at P1, P4, and P10 in the SVZ have an amoeboid shape and are positive for CD68 (representative cells: white arrowheads), whereas those at p30 have a more ramified shape and are negative for CD68. ***D***, The quantification of the number of Iba1$^+$ cells in the SVZ. ***d1***, Time course of the Iba1$^+$ microglia in the middle SVZ. The number peaked at P10. d2, d3, The comparison of the numbers of microglia among the rostral, middle, and caudal SVZ at P4 (***d2***) and P10 (***d3***). *$p < 0.05$ versus p1 or rost group (Tukey's test by ANOVA). Data are mean ± SEM. ***E***, The cell density of Iba1$^+$ microglia at different rostrocaudal levels at P1, P4, P10, and P30. The cell density of microglia in the SVZ paralleled with that of the number of microglia throughout a period of the observation. ***F***, The ratio of activated microglia in the SVZ (CD68$^+$/Iba1$^+$). During the experimental period, the highest ratio was obtained at P1. We confirmed the similar results in three independent experiments.

Results

We first investigated the distribution of microglia in the postnatal rat forebrain (Figs. 1 and 2). Sagittal sections were immuno-

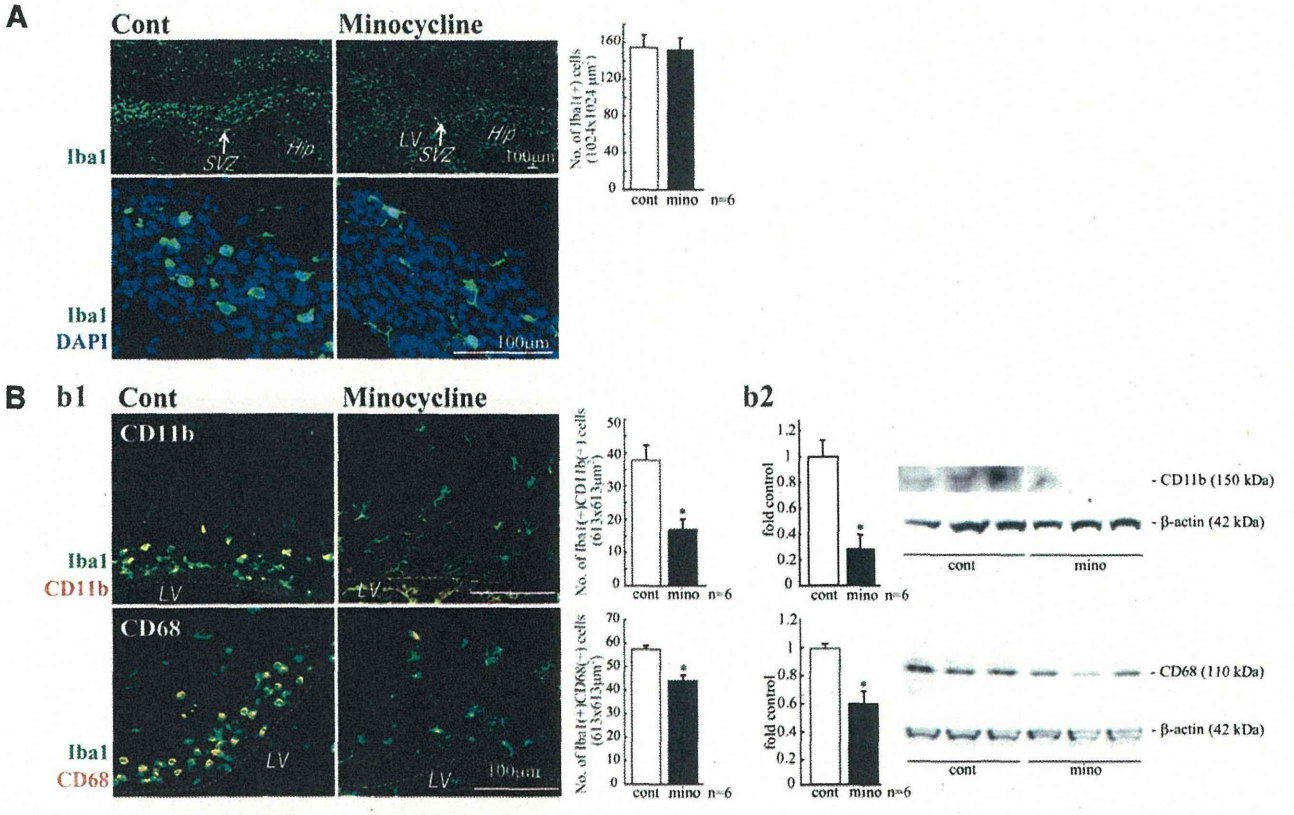

Figure 3. Minocycline suppressed microglial activation *in vivo*. ***A***, Effects of minocycline on the number of Iba1 $^{+}$ cells in the SVZ and their morphologies. Minocycline was administered by intraperitoneal injection for 3 d beginning at P2 (30 mg/kg/d, P2-P4, $n = 6$/group). Sagittal sections of minocycline-treated forebrains were immunostained for Iba1 (green) followed by DAPI staining (cyan). Although the number of Iba1 $^{+}$ microglia in the SVZ did not change (graph), their shape shifted from an amoeboid type to a more ramified type by minocycline (bottom). ***Bb1***, Effects of minocycline on the expression of activation markers and the morphologies of microglia. Sagittal sections of minocycline-treated forebrains were immunostained for Iba1 (green), and CD11b (red), and CD68 (red). Minocycline significantly decreased the number of cells positive for CD11b or CD68. The morphologies of the cells were also changed from amoeboid shape to more ramified shape. ***Bb2***, The significant decrease in the expression of CD11b and CD68 was confirmed by Western blotting of the SVZ as well. $*p < 0.05$ (Student's t test). Data are mean ± SEM. Similar results were obtained in three independent experiments.

stained with anti-Iba1, the marker for all microglia (green: microglia), and anti-GFAP antibodies (red: neural stem cells and astrocytes) at P1, P4, P10, P14, and P30. We found that a large number of microglia accumulated in the postnatal SVZ from P1 to P10 (Fig. 1*A*), especially at P4. The microglia in the VZ/SVZ at P1 and P4 display an amoeboid shape, whereas those outside the SVZ have a more ramified shape (Fig. 1*Aa2*). At P10, the number of microglia outside the SVZ had dramatically increased; the microglia in the VZ/SVZ remained amoeboid. At P14, the number of microglia had increased further and now ramified microglia were also observed in the VZ/SVZ. At P30, the numbers of microglia in the SVZ had decreased and most of the microglia had assumed a ramified shape. Further magnified images in Figure 1*Aa3* show that the shape of microglia in the SVZ changed gradually from amoeboid (P4) to ramified (P30). Figure 1*B* shows the expression of CD11b (Fig. 1*Bb1*) and CD68 (Fig. 1*Bb2*) in the SVZ microglia at P10. CD11b is potentially a marker for all microglia; however, its level is highly elevated by activation. CD68 is a marker for activated microglia. The levels of CD11b and CD68 are much higher in the amoeboid microglia in the SVZ (white arrowheads) than in the ramified ones outside the SVZ (black arrowheads), indicating that the SVZ amoeboid microglia have an activated phenotype.

To examine the developmental dynamics of microglia in the SVZ temporally and spatially, we examined the distribution of microglia in coronal sections that include rostral, medial, and caudal SVZ at P1, P4, P10, and P30 (Fig. 2). Each rostrocaudal level was determined according to a previous report (Suzuki and Goldman, 2003). Coronal sections were immunostained with anti-Iba1 (green: microglia) followed by DAPI staining (blue: cell nuclei) (Fig. 2*B*,*C*). The SVZ could be clearly delineated by its dense cellularity. From P1 to P10, a large number of microglia accumulated at all rostral, middle, and caudal levels. When we quantified the number of microglia in the SVZ, they gradually increased from P1 to P10, reached a maximum at p10, and decreased at P30 at all coronal levels (Fig. 2*B*,*D*, d1). Microglia displayed an amoeboid shape at P1, P4, and P10 but had become more ramified at P30 (Fig. 2*Cc1*). Among the different rostrocaudal levels, the number of microglia in the middle SVZ was significantly larger than in other levels at all ages (Fig. 2*D*, d2, d3). The changes in cell density (i.e., the ratio of Iba1 $^{+}$/DAPI $^{+}$) of microglia in the SVZ paralleled that of the number of microglia throughout the period of observation (Fig. 2*E*). We next examined immunostaining for CD68 in SVZ microglia. Figure 2*Cc2* shows representative images of double staining with anti-Iba1 and anti-CD68. At P1 and P4, most Iba1+ microglia in the SVZ were also positive for CD68. At P4, the CD68 signals became much stronger. At P10, a few microglia had appeared that had little CD68. At P30, double-positive cells were markedly decreased in number. The time course of the ratio of CD68 $^{+}$/Iba1 $^{+}$ cells is shown in Figure 2*F*: the highest ratio was obtained at P1. The ratios at P4 and P10 were almost equivalent and then were